First Structured Uranium-Based Monoliths Produced via Vat Photopolymerization for Nuclear Applications

Alice Zanini, Pedro Amador Celdran, Olaf Walter, Sara Maria Carturan,
*Jacobus Boshoven, Antonio Bulgheroni, Lisa Biasetto, Mattia Manzolaro, Rachel Eloirdi,**
Stefano Corradetti, and Giorgia Franchin**

Uranium plays an unquestionable role in the framework of nuclear physics, biology, and radiopharmacy. Moreover, uranyl ion UO_2^{2+} offers an immense variety of applications due to the unique photosensitivity of its complexes. The excited state of uranyl cation is indeed accessible under ultraviolet-visible (UV–vis) light, readily producing radical species UO_2^{2+*} upon light irradiation. Herein, an innovative synthesis protocol is presented to explore the use of uranyl cations as photocatalyst systems for photocurable sol–gel-based formulations, coupling the photochemical reactions of uranyl cations with photopolymerization-based additive manufacturing processes. Additive manufacturing has nowadays revolutionized the production of complex structures with arbitrary geometries and has opened up enticing opportunities for innovative technological breakthroughs and highly tailorable systems. The fabrication of micro-architected components is shown via vat photopolymerization, namely, the Digital Light Processing technique, and -3D) printed parts are converted into uranium dicarbide (UC_2)/carbon nanocomposite upon carbothermal reduction. This uranyl-mediated additive manufacturing process constitutes the first application of the synergistic role of uranyl motifs in a photopolymer platform, demonstrating for the first time the possibility to directly pattern uranium-based materials in complex structures.

1. Introduction

Over the past decades, the surge in interest in rapid prototyping has prompted the expansion of the use of Additive Manufacturing (AM) technologies in frontrunner sectors of modern industries, such as aerospace, automotive, energy production, and medical applications. AM allows for innovative design and hitherto untenable geometric complexity, thus providing a valuable methodology to realize high-performance components that are often fabricated for extreme operating conditions. These complex-shaped components typically exhibit multi-material layouts and cellular structures with several combinations of functional attributes, such as extreme temperature resistance, ultra-light weight, and high reliability.[1] Among the sheer diversity of applications, the use of AM for high-quality and customized near-net-shaped components, along with cost and waste reduction, has recently attracted extensive attention in the nuclear field.[2,3] AM technologies have been explored for the production of reactor internal components in nuclear power plants[4,5] and the enormous design freedom has charted a path for the development of innovative nuclear fuel architectures,[6] albeit still limited to a concept rather than a practical approach. Additive manufacturing technology enables to purposefully engineer the porosity of the printed components, potentially leading to significant improvements in both thermomechanical performance and physical functionality of actinide systems for nuclear fuels applications. Indeed, the maximum fuel temperature may largely benefit from the presence of functional porosity, as for annular

---

A. Zanini, L. Biasetto, G. Franchin
Department of Industrial Engineering
University of Padova
Via Marzolo 9, Padova 35131, Italy
E-mail: giorgia.franchin@unipd.it

P. A. Celdran, O. Walter, J. Boshoven, A. Bulgheroni, R. Eloirdi
Joint Research Centre
European Commission
Karlsruhe, Germany
E-mail: rachel.eloirdi@ec.europa.eu
S. M. Carturan, M. Manzolaro, S. Corradetti
INFN-Laboratori Nazionali di Legnaro
Viale dell'Università 2, Legnaro 35020, Italy
E-mail: stefano.corradetti@lnl.infn.it
S. M. Carturan
Department of Physics and Astronomy
University of Padova
Via Marzolo 8, Padova 35131, Italy

fuel forms;[7] furthermore, the design of void space can mitigate the swelling induced by the formation of fission gas within the fuel microstructure and improve its transport via interconnected architectures.[6] Moreover, the ability to pattern 3D periodic structures has imposed a new set of paradigms for the fabrication of complex-shaped parts with outstanding mechanical strength, lightweight design, and improved thermal conductivity, as reticulated components (i.e., trusses, honeycombs, ordered lattices) can easily dissipate high-intensity heat due to the larger surface area and porosity, thus demonstrating great potential in developing components for extreme heat resistance applications.[8,9]

As one of the most unstable naturally occurring actinides,[10] uranium has utterly pervaded the global politics and economy of energy resources, unveiling groundbreaking opportunities for energy production in nuclear power plants. The use of uranium-derived materials as nuclear fuels has rapidly grown due to the potential of producing components with high uranium density and promising thermal properties, with uranium generally employed in the form of uranium dioxide UO_2 fuel pellets.[11–13] Nevertheless, novel uranium-based materials represent attractive candidates, such as uranium mononitride[14] and uranium silicide U_3Si_2,[15] which exhibit high fissionable density and enhanced thermal conductivity with respect to UO_2. In addition, uranium carbides U_xC_y hold great promise in the framework of nuclear physics, as U_xC_y materials show higher compatibility with carbon-based high-temperature matrix elements (i.e., silicon carbide, graphite, and zirconium carbide) compared to oxide fuels, while retaining fission products in a more thermodynamically stable carbide phase at elevated temperatures.[16–18] Additionally, uranium carbides have emerged as the reference target material for the production of a wide variety of radioactive species used in nuclear medicine applications. Radioactive isotopes have gained increasing interest as a frontrunner for the production of innovative radiopharmaceuticals, allowing for precise delivery of therapeutic doses and the development of novel molecular-tailored treatments.[19,20] In this regard, ISOL (Isotope Separation On-Line) facilities have received growing attention as an established technique to produce radioactive ion beams (RIBs), exploiting the interaction between a particle beam and the target material, with great interest for actinide carbides exhibiting open porosity and high specific surface area to maximize the isotope release.[21–24] A broad variety of radioactive ion beams has been produced from uranium carbide targets using the ISOL technique, including Fr,[25] Cs,[25,26] Kr, Y, Ru, Sb, Te, La, Ba, Ce,[26] Xe,[26,27] Al,[27] Ga and In,[28] I,[26,29] Sr and Sn.[24,26] The RIB intensity I_{RIB} can be expressed as:[21]

$$I_{RIB} = \sigma_i(E^*) \cdot N_{target} \cdot I^* \cdot \varepsilon \tag{1}$$

where $\sigma_i(E^*)$ is the nuclear production cross-section of a desired isotope i, by the interaction of a particle of energy E^* and the target nucleus, N_{target} is the number of target nuclei, I^* is the driver beam intensity and ε is the overall efficiency. The overall efficiency ε has several contributions of which the one strictly related to the material is called release efficiency and depends on diffusion within the material grains and effusion through pores. This means that the material density, its microstructure/nanostructure so as its morphology in terms of pores amount and interconnectivity degree all represent specific

features that have been deeply investigated in the last twenty years.[30,31]

The extensive demand for synthetic approaches in the framework of nuclear applications has fostered significant efforts in the design of tailored target materials, shedding some light on the tremendous potential of actinide-derived chemistry.[32–34] Among the several actinyl cations, uranyl(VI) is the most thermodynamically stable and widely explored, forming a nearly linear O=U=O structure comprising strong covalent bonds between uranium and two oxygen atoms.[35] The unique potential of the uranyl cation UO_2^{2+} is related to the photochemical properties of its complexes.[33,34] Specifically, the photoexcitation under UV and visible light of the uranyl cation results in the formation of chemically reactive radical species UO_2^{2+*} that can act as photocatalysts[34–36] and initiate photopolymerization reactions without the utilization of photoinitiator systems. Photoinitiators play a crucial role in photopolymerization processes as they control the curing rate. However, these compounds are typically expensive, harmful, oxygen-sensitive, and possess low water solubility, hence posing substantial challenges to solubility in water-based photocurable systems.[37–39] Herein, we propose the use of uranyl motifs as a photocatalyst plus uranium source for the synthesis of photocurable water-based sol–gel inks from uranyl nitrate, thus overcoming the limitations related to poor compatibility between photoinitiator and photocurable formulations and ensuring high purity of the component (which would reflect on the purity of the produced isotope beam). This enables the shaping via vat photopolymerization, namely Digital Light Processing (DLP), of the printable feedstock comprising the photopolymer poly(ethylene glycol) diacrylate (PEGDA M_n 575) as the photocurable matrix that can be photoactivated in a uranyl-mediated and photoinitiator-free photopolymerization process.

2. Results and Discussion

2.1. Ink Synthesis and 3D Printing of U-Based Structures

A one-pot sol–gel synthesis was developed to precisely engineer the chemical design and enable the preparation of photocurable formulations that possessed efficient printability for DLP (**Figure 1**). Indeed, the coupling of additive manufacturing and the sol–gel route enables the development of a distinctive pathway that exploits the full potential of both techniques and allows to widen the realm of organic and inorganic materials that can be patterned.[40–45] The utilization of liquid feedstocks as printing inks ensures an intimate and homogeneous mixing of the components, avoiding the extensive shortcomings derived from powder-based formulations, such as particle sedimentation, viscosity constraints, light-scattering and absorbing effects that inherently limit the resolution and final quality of the printed components.[46–49] To ensure high chemical homogeneity of the metal salt-based formulation, citric acid (CA) is herein introduced in the solution system as the complexing agent in a modified Pechini process.[50,51] The synthetic approach involves the formation of uranyl-citrate complexes, followed by an esterification reaction with sucrose as the polyhydroxy compound and polymerization agent to create an extended covalent polymeric structure where the metal species are finely entrapped
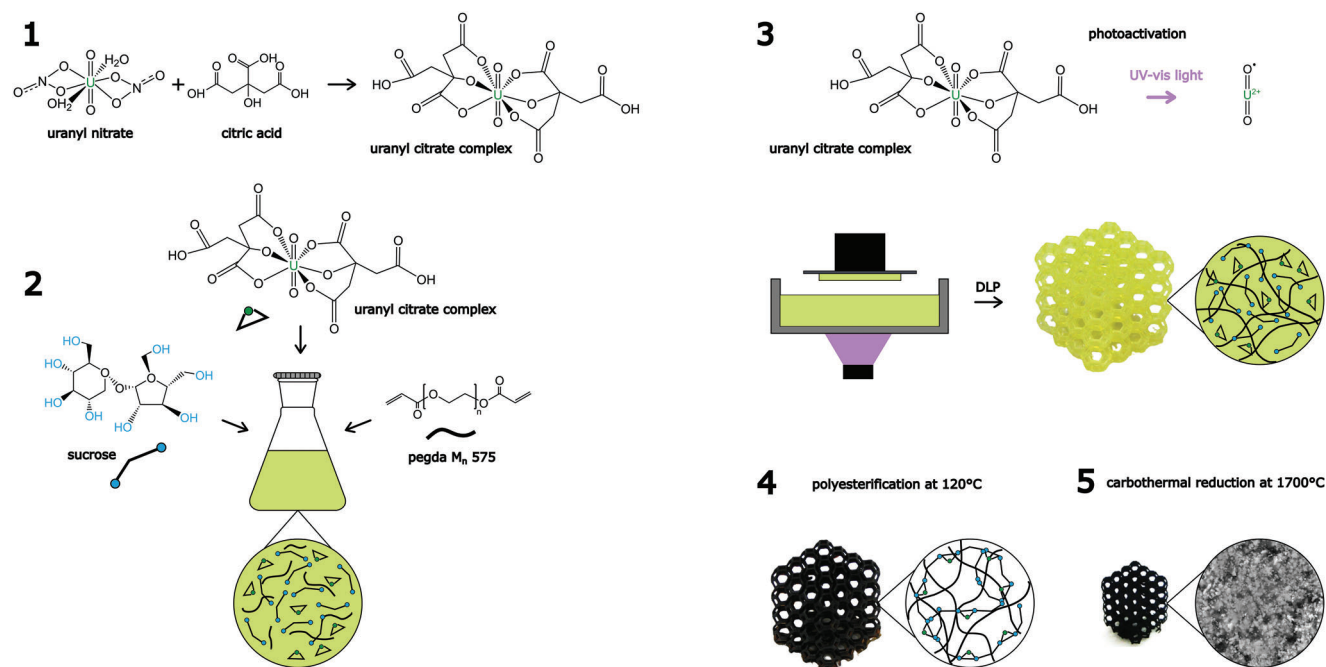
2406916 (2 of 10)

Figure 1. Schematic of the synthetic protocol for the fabrication of uranium-based complex components. 1) Complexation of uranyl nitrate with citric acid. 2) Preparation of the photocurable sol–gel-based formulation using uranyl-citrate complexes, sucrose, and PEGDA M_n 575. 3) Photoactivation of uranyl-citrate complexes by UV–vis light exposure and fabrication via DLP. 4) Polyesterification at 120 °C in air to enable the formation of the covalent crosslinked network wherein U ions are entrapped. 5) Carbothermal reduction at 1700 °C under Ar atmosphere.

throughout the network.[50,52,53] Sucrose hydrolyses into two monosaccharides, glucose and fructose, in aqueous solutions.[54] In the presence of nitrate groups from the uranyl nitrate precursor, the two monosaccharides can be oxidized and converted to saccharic acid, gluconic acid and trihydroxybutiric acid,[55,56] containing carboxylate and hydroxyl groups that are involved in the complexation of the metal building blocks as well as esterification to form the branched polymeric matrix. In addition, citric acid[51] and sucrose[57] act as carbon precursors, thereby providing the carbon content for a subsequent carbothermal reduction into uranium carbide-based material. The formation of the rigid organic network upon esterification allows for the immobilization of the uranyl ions in the polymeric structure, as the metal complexes are directly bonded with sucrose-derived species, therefore preventing segregation and precipitation of aggregates. Moreover, the entrapment of the uranyl ions within the matrix ensures intimate contact with the carbon precursors at a molecular scale, providing shorter diffusion distances and thus improving the carbothermal reduction process. The molar ratio between the complexing agent citric acid and the polymerization agent sucrose was set to 4 (U:CA:sucrose = 1:2:0.5), as different ratios were also preliminarily explored but resulted in a larger permanence of UO_2 domains upon heat treatment at 1700 °C, suggesting that the carbothermal reduction into UC_2 was significantly less efficient (Figure S1, Supporting Information). The amount of photopolymer PEGDA was determined using an iterative approach, aiming at minimizing the content of the photocurable constituent to ensure adequate printability response (i.e., high fabrication speed and survival after printing), while maximizing the solid loading in the sol–gel formulation. Preliminary studies aiming at the op-

timization of the synthetic protocol were performed on samples prepared via casting. A commercial DLP printer (Asiga MAX X UV385, Asiga, Australia) was then used to directly create 3D complex-shaped structures in a layer-by-layer fashion (**Figure** 2a). The printed components display high accuracy with respect to the - (CAD) model upon sintering (Figure 2b), exhibiting fully dense struts with high-fidelity features. Slight deviations in the struts' thickness may be attributed to the CAD slicing process and to the samples' cleaning procedure. The exceptional printing resolution that can be afforded using the as-developed formulation is further probed by the observation of the pixel shape within the sintered struts (Figure 2b), revealing that shrinkage phenomena upon carbothermal reduction allow to reach a high spatial resolution of ≈12 µm.

2.2. Photoactivation of Uranyl-Citrate Complexes

Uranyl cations UO_2^{2+} are chemically robust species and the strong covalent character of the oxo groups U-O_{yl} imparts significant limitations to the equatorial plane in the coordination environment.[58] Moreover, UO_2^{2+} species easily form very stable complexes with citric acid, resulting in water-soluble and mobile hexavalent uranyl species. Citric acid (H_3Cit) is a hydroxytricarboxylic acid comprising one hydroxyl group and three carboxyl groups that can readily serve as binding sites; the configuration of these coordination sites imposes steric constraints on the complexation of the uranyl cation and three groups can bind at most to the same ion, while the non-bonded group(s) can potentially act as a bridging site to another ion.[59] Therefore, for the
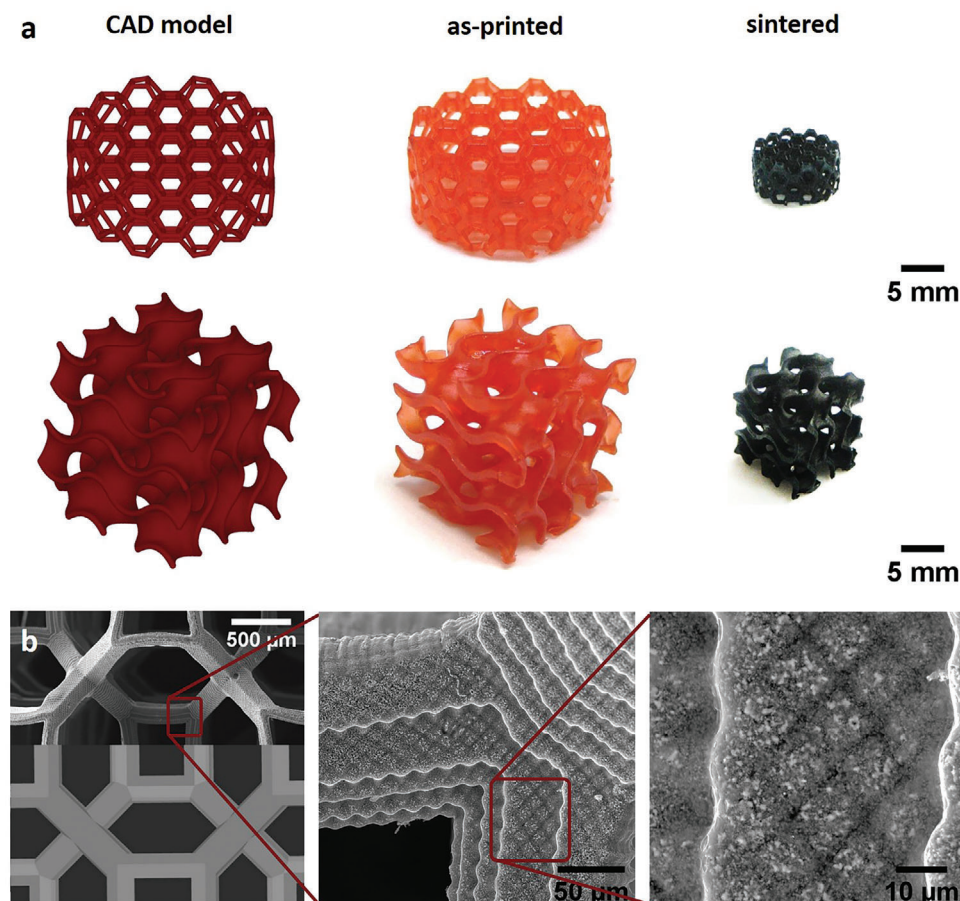
Figure 2. Fabrication of uranium-based components via DLP. a) CAD model and optical images of the printed components as-printed and upon sintering at 1700 °C for 24 h: discoidal Kelvin cell-derived (up) and gyroid (down) structures. The red color is due to the incorporation of the photoabsorber. b) Comparison between CAD model (down) and SEM image (up) for a sintered component. The pixel shape is clearly visible in the sintered printed strut at higher magnifications.

uranyl-citrate complexes herein used, only the hydroxyl and two carboxylate groups are involved in the complex formation, with several studies suggesting that deprotonation of the hydroxyl group occurs upon metal complexation due to the strong interaction between the metal ion and the functional group.[60] Similarly to that previously proposed,[59] the formation of uranyl(VI)-citrate complexes (CA:U = 2:1) can be described as follows:

$$UO_2^{2+} + 2Cit^{3-} \rightarrow UO_2\left(HCit_{-H}\right)_2^{4-} \qquad (2)$$
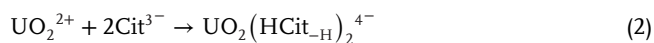
UV–vis absorption spectrum (**Figure 3**b) for an aqueous solution of uranyl nitrate hexahydrate (0.066 M) reveals the presence of the characteristic maximum peak at 413.8 nm, and a steep increase in the molar absorptivity toward the UV range, as previously reported.[61] The molar absorptivity for the pure uranyl cation in aqueous solution is 7.12 M^{-1} cm^{-1} at 413.8 nm, in good agreement with previous works indicating a molar extinction coefficient in the range 7–10 M^{-1} cm^{-1} at the same wavelength.[62–64] The coordination of uranyl(VI) by citric acid in the photocurable formulation results in an increase of the molar absorptivity, poor band definition, and a slight bathochromic shift of the main absorption bands with respect to the pure

uranyl species in water, as typically observed for other uranyl(VI) complexes.[63,65] Specifically, if the coordination mechanism involves iodate[63] or carboxylic acids, such as citric acid, the complexation results in a shift of the absorption maximum to higher wavelengths, whilst the use of hydroxamic acids leads to a blue shift.[66] Herein, the bathochromic shift indicates that the coordination environment is ruled by the carboxyl oxygen atom from the carboxylic ligand. The molar absorptivity for our complex system at the absorption maximum is 31.02 M^{-1} cm^{-1}, exhibiting a four-fold increase with respect to that for pure uranyl cation. Moreover, the complexation with citric acid leads to a shift to longer wavelengths of the steep absorption edge to the region below 350 nm, as previously observed.[62] The increase of molar absorptivity can be correlated with the formation of polynuclear species and oligomerization of UO_2^{2+}, such as dimeric and trimeric complexes, whereas hydrated species are dissolved in the form of monomeric units in the uranyl aqueous solution.[67] Furthermore, the uranyl aqueous solution exhibits less intense bands and a good band definition, hinting at a higher symmetry of the uranyl structures and thus probing the formation of monomeric structures over oligomers.[68] The citrate ligands become anchored to the uranyl
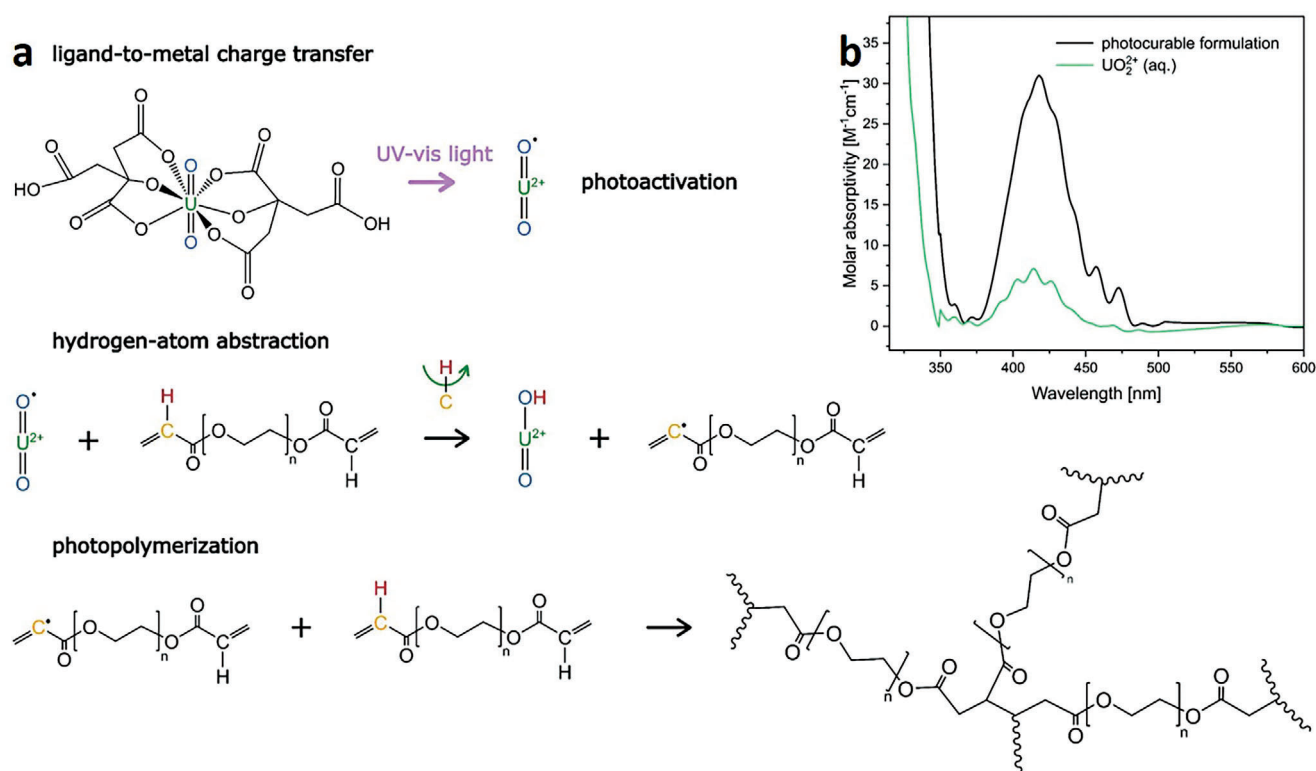
ADVANCED
SCIENCE NEWS

www.advancedsciencenews.com

ADVANCED
FUNCTIONAL
MATERIALS

www.afm-journal.de

Figure 3. Uranyl-mediated photocleavage of PEGDA M_n 575 to induce the photopolymerization process. a) Proposed mechanism: 1- Photoactivation of the uranyl-citrate complex via ligand-to-metal charge transfer. 2- Formation of the carbon-based radical through hydrogen abstraction by the uranyl radical complex. 3- Photopolymerization process. b) UV–vis spectra of photocurable formulation and aqueous solution of uranyl nitrate.

moiety and modify its symmetry, leading to the weakening of linear O═U═O bonding, increased bond lengths and polarizability within the uranyl moiety complex.[34,69] Upon exposure to UV light, the photocurable formulation transitions from a liquid solution to a solid structure, as shown in Figure 2a (red). Plausible mechanisms that can describe the uranyl-mediated photocleavage of PEGDA are outlined in Figure 3a. We posit here that telechelic photopolymer PEGDA M_n 575 g mol^{-1} undergoes rapid covalent crosslinking in a uranyl-mediated reaction, as the uranyl-citrate complexes are activated upon light irradiation through a ligand-to-metal charge transfer from the highest filled 2p-orbitals of oxygen to the non-bonding 5f-orbitals of uranium.[34,35] The highly excited state UO_2^{2+*} can efficiently abstract hydrogen atoms from inactivated aliphatic groups to generate primary carbon-centred radicals through a C─H bond cleavage, as already investigated for proteins,[70] peptides[71] and alkane C─H bonds.[36] Then, the formed radicals attack the terminal alkene groups contained in the photopolymer backbone and initiate the chain-growth polymerization. Hence, the uranyl motifs allow for the activation of the acrylate functionalities in a free-radical photopolymerization process to create a distinct network upon photocleavage of the double carbon bonds. Further, upon heating at 120 °C, an interpenetrating network is formed comprising the uranyl-citrate complexes that undergo polyesterification reactions with the sucrose-derived species, as depicted in Figure 1.

2.3. Morphology and Microstructural Characterization

The hybrid organic-inorganic 3D-printed components are then thermally treated in an argon atmosphere at 1700 °C to remove the organic constituents, leading to the black samples shown in Figure 2a. The conversion process of the uranyl complexes within the photocured network to metal carbide is greatly affected by the carbothermal reduction time, as shown in **Figure 4a**. Indeed, the main diffraction peak intensity of UO_2 ($\approx$28.3°) diminishes with respect to that of UC_2 ($\approx$29.4°) as the reaction time at 1700 °C increases, revealing a complete conversion of the UO_2/C nanocomposite into tetragonal α-UC_2 with a crystallite size of 56.6 nm, uranium monocarbide UC and graphite after a dwelling time of 24 h at 1700 °C. In contrast, the carbon peak ascribed to the graphite phase ($\approx$26.6°) becomes progressively larger in intensity with increasing time at 1700 °C, indicating that residual carbon in the form of graphite is generated during the pyrolysis of the organic compounds acting as carbon source. The presence of excess carbon has already been demonstrated to impart great improvements in terms of thermomechanical and release properties for ISOL target materials,[57,72] and allows to limit the grain size of uranium carbide.[73] The carbothermal reduction process can be envisioned as a stepwise conversion, with an initial surface reaction involving UO_2 particles covered by a coherent layer of UC_2, followed by a diffusion-controlled mechanism from the surface to the UO_2–UC_2 interface.[74] Then, the
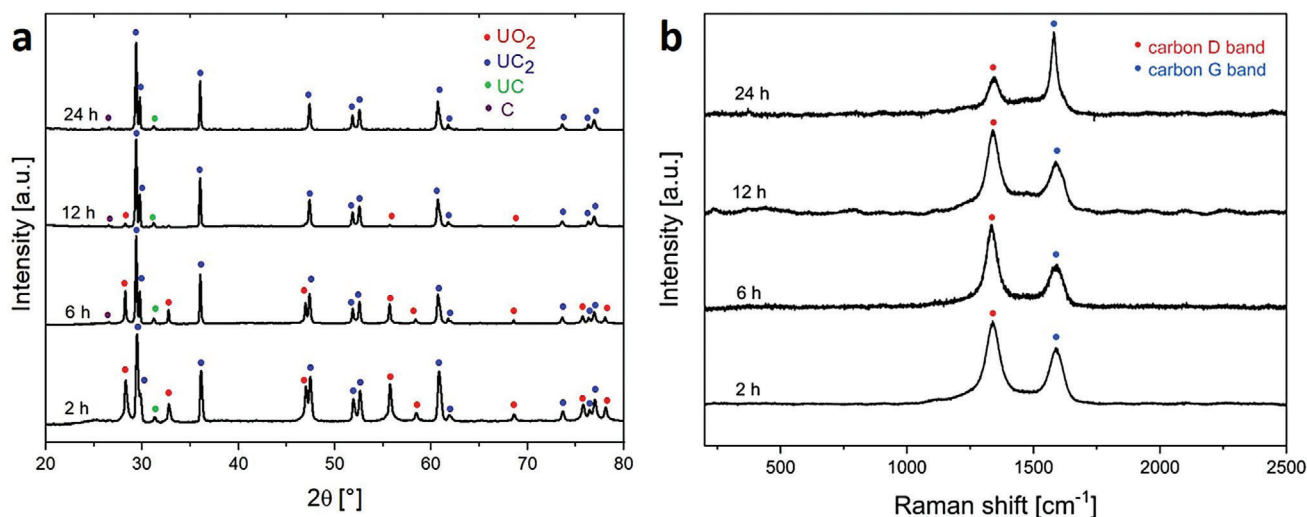
Figure 4. Structural characterization of U-based printed components. a) XRD patterns and b) Raman spectra for different sintering times at 1700 °C in argon.

carbothermal reduction proceeds at the interface toward the unreacted center, whilst the formed carbon monoxide CO readily diffuses through the converted layer.[75] Furthermore, the presence of face-centered cubic UC is detected for all the different tested times during the carbothermal reduction of UO_2. The Raman spectrum (Figure 4b) shows the presence of two characteristic peaks, the D band at 1339 cm^{-1} and the G band at 1588 cm^{-1}: the former is a disorder-induced feature, while the G band is a signature mode of carbon-based materials.[76] The intensity ratio I_D/I_G is widely used to determine the degree of disorder, as an increase in this value is correlated with the presence of structural defects. Herein, the strong intensity ratio (1.46) at 2 h hence suggests the formation of turbostratic graphite domains, although not detected in the X-ray diffraction (XRD) pattern. Noticeably, uranium carbide UC_x has no Raman active modes, thereby only the carbon-derived modes can be observed in the Raman spectra.[73] As the sintering time is increased to 6 h, the strong intensity ratio I_D/I_G (1.82) indicates an increasing disorder within the graphite structure.[76] A significant increase in the lattice parameter of UO_{2+x} (a = 5.469 Å) as well as crystallite size (48 nm) suggests a decrease in the hyper-stoichiometry of UO_2, as some oxygen atoms diffuse from the interstitial sites of the uranium dioxide structure.[73] Moreover, the clear increase in the lattice parameters for UC (a = 4.959 Å) and UC_2 (a = 3.524 Å, c = 5.990 Å) might be related to the diffusion and positioning of atom carbons from the forming turbostratic domains to the UC_x phases. As the carbothermal reduction proceeds at 12 h, the decrease in the crystal size of the highly disordered turbostratic graphite (37.4 nm) and uranium dioxide (43.4 nm) can be attributed to the conversion of $UO_2 + C$ into novel smaller UC_2 domains via a diffusion-controlled mechanism. The negligible variations in the lattice parameters of the UC_X phases upon sintering at 12 h suggest that structural changes predominantly occur during the very early stages of the carbothermal reduction process, while for longer reaction times, the main mechanisms driving the sintering process are coarsening and grain growth, as revealed by the increased crystallite sizes for all the three phases

(**Table 1**). As reported in Table 1, the samples pyrolyzed at 1700 °C for 24 h in argon exhibit a weight loss of 86.8%, in good agreement with the predicted theoretical value of 84.8% (Table S2, Supporting Information). The largest weight loss for 24 h suggests that the residual uranium dioxide can be successfully converted into UC_x as the oxygen is removed from the system as gaseous species, that is, CO, during the final stages of the densification process. Indeed, for a sintering time of 24 h, the diffraction peaks of UO_2 are no longer detected, revealing that the carbothermal reduction is close to completion. The final nanocomposite material thus comprises hyper-stoichiometric uranium monocarbide, uranium dicarbide, and graphitic domains. Moreover, the Raman intensity ratio of weak band D to the strong band G (0.43) suggests a high degree of ordered graphitic carbon, also confirmed by the lower interlayer distance (3.354 Å), revealing that the long sintering time imparts structural orderliness to the carbon domains. The external morphology of the uranium carbide/carbon nanocomposites was investigated via scanning electron microscopy (SEM) and energy dispersive X-ray spectroscopy (EDX) analysis. SEM images (**Figure 5a,b**) show that 3D printed components retain their complex architectures upon sintering at 1700 °C, while revealing the presence of internal porosity at higher magnifications. Throughout the carbothermal reduction process, the printed components undergo a volumetric shrinkage of 90.5% for 24 h at 1700 °C, leading to internal pore formation with a- (BET) specific surface area of 59.3 m^2 g^{-1}. This value is well above the 11–32 m^2 g^{-1} specific surface areas that have been previously reported for UC_x ISOL targets prepared in the form of pressed pellets,[77] hence revealing great potential as target components. Furthermore, isotropic linear shrinkage (≈50–55%) is measured for the printed parts upon heat treatment at different sintering times, with a variation between the two measurements along the x–y plane and the z direction below 3.5% (Table S1, Supporting Information). A theoretical model based on the complete conversion of the uranium and carbon precursors into fully dense UC_2/C was developed and it predicts final volumetric and linear shrinkages of 95.5% and 64.4%, respectively. The

**ADVANCED
SCIENCE NEWS**

www.advancedsciencenews.com

**ADVANCED
FUNCTIONAL
MATERIALS**

www.afm-journal.de

Table 1. Crystallographic data, weight loss, and shrinkage for the samples at different sintering times.

Sintering time [h]	Phase	Lattice parameter [Å]	Crystallite size [nm]	I_D/I_G	Weight loss [%]	Volumetric shrinkage [%]
2	UO_2	5.460 ± 0.007	28.8 ± 1.2	1.46	85.1 ± 0.2	_a)
	UC	4.945 ± 0.001	33.2 ± 0.1			
	UC_2	$a = 3.514 \pm 0.001$	32.1 ± 1.1			
		$c = 5.973 \pm 0.001$				
6	UO_2	5.469 ± 0.002	48.0 ± 4.3	1.82	85.3 ± 2.5	90.7 ± 1.8
	UC	4.959 ± 0.001	36.0 ± 0.1			
	UC_2	$a = 3.524 \pm 0.001$	53.9 ± 2.3			
		$c = 5.990 \pm 0.002$				
	C	6.712 ± 0.001	46.7 ± 0.1			
12	UO_2	5.468 ± 0.001	43.4 ± 4.4	1.81	86.0 ± 0.5	90.2 ± 0.8
	UC	4.962 ± 0.001	35.4 ± 0.1			
	UC_2	$a = 3.525 \pm 0.001$	49.8 ± 3.8			
		$c = 5.993 \pm 0.002$				
	C	6.716 ± 0.001	37.4 ± 0.1			
24	UC	4.960 ± 0.001	38.0 ± 0.1	0.43	86.8 ± 0.1	90.5 ± 1.5
	UC_2	$a = 3.525 \pm 0.001$	55.8 ± 5.9			
		$c = 5.993 \pm 0.001$				
	C	6.708 ± 0.001	56.6 ± 0.1			

a) After thermal treatment at 1700 °C for 2 h, the samples exhibited poor mechanical integrity, and therefore volumetric shrinkage measurements were not reliable.

discrepancy between the theoretical and experimental results for the shrinkage values further confirms the formation of porous frameworks, with an estimated strut porosity (i.e., the porosity of the material constituting the struts of the printed and sintered lattices) of 19.5% (see Supporting Information for additional discussion). While ongoing research is striving to design high-performance components with spatially varying features that can be used as ISOL targets, we propose the 3D printed discoidal Kelvin cell-derived component in Figure 2a as a proof-of-concept study. The lattice structure exhibits a geometrical porosity (by CAD design) of 89.9%, resulting in a final total porosity for the printed material upon carbothermal reduction of 91.9% (Supporting Information). Thus, the utilization of additive manufacturing allows to greatly enhance the final porosity, which was previously limited to 29% for UC_x-graphite nanocomposite prepared as pellets from pressed powders.[22] With this approach, components ranging from ≈20% porosity (i.e., dense pellets with no added geometric porosity) to > 90% can be produced. The fabrication of cellular structures by purposefully designing the distribution of the volume fraction can in fact ensure even higher porosity, thereby providing larger escape pathways for the release of the radioisotopes and enabling the integration of structural complexity within the material performance under extreme operating conditions.

A homogeneous distribution of uranium, carbon and oxygen can be seen throughout the 3D-printed component sintered at 1700 °C for 24 h, without the presence of segregation areas (Figure 5c). In spite of the absence of diffraction peaks attributed to oxide-based compounds, the presence of oxygen must be accounted for, as this contamination might be less than the detection limit for the XRD instrument but could be effectively measured for the EDX compositional analysis, as shown in the ele-

mental maps. EDX semi-quantitative analyses show a chemical composition of 64.84 wt% U, 32.50 wt% C, 2.66 wt% O after sintering at 1700 °C for 24 h (Figure 5c). Therefore, EDX analyses reveal a final stoichiometry U:C of 1:9.93, in agreement with the results from the chemical analysis content (31.3 ± 2.2 wt% C, U:C = 1:9.01).

3. Conclusion

A versatile methodology is reported for the preparation of a sol–gel formulation to fabricate complex-shaped uranium carbide/carbon nanocomposites via the Digital Light Processing (DLP) technique. The chemical pathway involves the UV–vis light photoactivation of the uranyl ions, herein exploited for the first time for the photocleavage of alkene bonds thereby triggering photopolymerization reactions to fabricate complex 3D parts. The geometrical freedom here demonstrated opens the door to purposeful tuning meant to optimize the release efficiency of RIBs by controlling the struts densities (via specific design constraints and sintering conditions) so as the amount, shape and interconnectivity degree of pores at different scales. Preliminary investigations reveal promising outcomes in terms of specific surface area (59 m^2 g^{-1}) and porosity (ranging from 19.5% to 91.9%), thus paving the way for future advances in the framework of the ISOL method for the production of radioisotopes. In addition, this approach has demonstrated great potential in the manufacturing of 3D reticular structures that can provide novel strategies for the production of components relevant to the nuclear industry, such as nuclear fuel forms. The inherent flexibility of this sol–gel route allows to readily extend its utility to other uranium-based compositions, such as uranium dioxide, charting
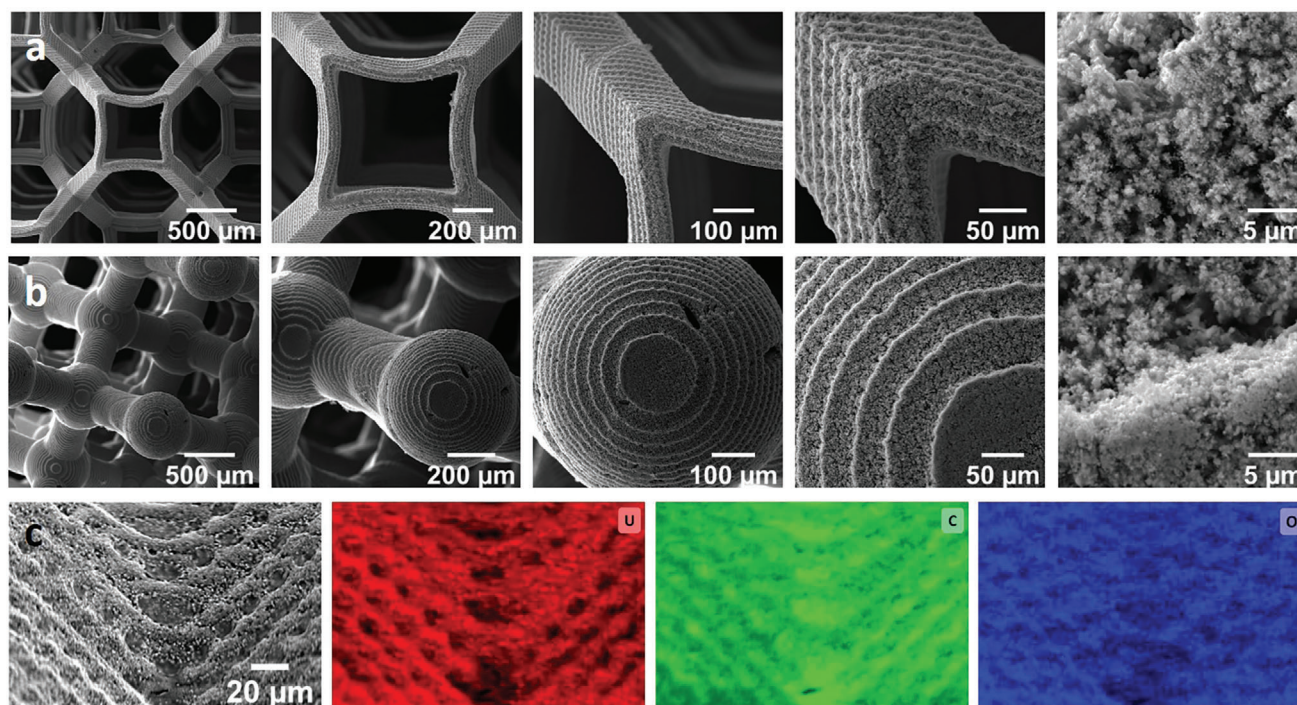
Figure 5. Chemical and morphological characterization of the printed components. a) SEM images of representative complex parts upon carbothermal reduction using secondary electrons. b) SEM and EDX mapping images of the uranium carbide/carbon nanocomposite sintered at 1700 °C for 24 h.

a path forward for the development of enticing applications for 3D printable micro-architected uranium complexes as valuable catalysts and novel advances in the field of molecular biology, nuclear medicine and physics.

4. Experimental Section

Synthesis: Uranyl nitrate hexaxydrate (International Bioanalytical Industries, Inc.) (1.67 g) was dissolved in 3 mL of H_2O and mixed for 20 min at 1000 rpm until a homogeneous solution was obtained. The citric acid (Sigma-Aldrich, ≥99.5%) (CA:U = 2:1) is then added to the sol and mixed to give a clear and yellowish solution for 30 min; sucrose (Sigma-Aldrich) (sucrose:U = 0.5:1) is then added and stirred to give a homogeneous solution. After 10 min, 4.308 g of a PEGDA M_n 575 (Sigma Aldrich) solution (60 wt% in H_2O) is blended with the uranyl-containing sol and left to stir for an additional 30 min. The synthesis was performed at ambient temperature and all the reagents were used as-received. Moreover, to prevent abrupt photoexcitation of uranyl cations and hence the formation of reactive radicals that can initiate photopolymerization processes within PEGDA M_n 575, the vessel containing the forming sol is wrapped with aluminum foil. Additionally, a photoabsorber (2-[(E)-(2-Methoxyphenyl)diazenyl]naphthalen-2-ol, Sudan Red G, Tokyo Chemical Industry – TCI) (0.027 wt% referred to the weight of the final solution) was added to the formulation to improve the printing resolution.

Additive Manufacturing via DLP: Uranium-based components were printed on a DLP 3D printer (Asiga MAX X UV385, Asiga, Australia) at the Joint Research Centre in Karlsruhe (Germany), European Commission. The layer thickness was adjusted at 50 μm and each layer was photocured for 1–3 s with a light intensity of 29 mW cm^{-2} using a UV–LED light source of 385 nm. The printing parameters can be found in Table S4 (Supporting Information). Working curves were obtained by measuring the thickness of 100 μL of photocurable ink with a digital caliper

upon UV-photoirradiation for different exposure times (Figure S5, Supporting Information). Moreover, additional specimens were fabricated in the form of monoliths (10 × 10 × 4 mm) via the casting process, using a curing box (Anycubic Photon Mono SE). After 3D printing, the printed components were carefully removed from the building platform, then cleaned from the unreacted residue using compressed air, ethanol, and then wiped with absorbing paper. The STL models printed in this work were downloaded from https://www.thingiverse.com and the following authors are acknowledged: ProFab3D for the structure printed in Figures 1, 2b, 5a,c, and Figures S3 and S4 (Supporting Information) (https://www.thingiverse.com/thing:2522147, license CC BY), pmoews for the diamond cell in Figure 5b (https://www.thingiverse.com/thing:13601, license CC BY), alpheccar for the gyroid structure printed in Figure 2a and S4 (Supporting Information) (https://www.thingiverse.com/thing:2403294, licence CC BY-NC-ND). Dr. Marco Pelanconi (Hybrid Materials Laboratory – SUPSI) is greatly acknowledged for the development of the CAD model of the discoidal Kelvin cell-based structure in Figure 2a.

Post-Processing Treatment: After printing, the fabricated samples were dried at 120 °C for 15 h in the air to promote polyesterification reactions between the uranyl-citrate complexes and sucrose.

Carbothermal Reduction: The dried 3D-printed components were thermally treated in a two-step carbothermal reduction. The first step involves a heating ramp of 200 °C h^{-1} from ambient temperature to 1000 °C under argon atmosphere, 2 h of dwelling, and a cooling ramp 200 °C h^{-1} from 1000 °C to ambient temperature (Figure S2, Supporting Information). The samples were placed in a tube furnace type FRO-H-2-120/250, equipped with a quartz tube. During the second step, the samples were treated in an annealing furnace (Degussa Type VSL) under an argon atmosphere, according to the following schedule: temperature ramp 1 °C min^{-1} from ambient temperature to 700 °C, 2 h of dwelling, temperature ramp 2 °C min^{-1} from 700 °C to 1700 °C, 2 h of dwelling, temperature ramp 3 °C min^{-1} from 1700 °C to ambient temperature.

Materials Characterization—XRD: Powder XRD patterns were collected using a Bruker D8 diffractometer (Bruker AXS GmbH, Germany) mounted in a Bragg-Brentano geometry with Cu Kα radiation at 40 kV and

40 mA in a radiation protection glovebox. The XRD patterns were recorded in a 2θ range from 20 to 80 °C with a scan step of 0.013° and the average crystallite size was estimated from the XRD line broadening using the Scherrer equation.[78]

Materials Characterization—Raman: Raman spectra were recorded with a Horiba T64000 spectrometer (Horiba Jobin-Yvon, France) in a radiation protection glovebox, operating with a solid-state laser emitting at 532 nm (Cobolt Samba 1500). The Raman spectrometer is equipped with a low noise liquid nitrogen cooled Symphony detector and 1800 grooves mm^{-1} grating.

Materials Characterization—Spectroscopy: UV–vis spectra were collected using a Cary 5000 spectrophotometer (Agilent Technologies, CA) in polystyrene cuvettes of 10-mm thickness.

Materials Characterization—SEM-EDX: The surface morphology of the printed samples upon carbothermal reduction was characterized by a ThermoFisher Scientific Quattro S scanning electron microscope (SEM) in a radiologically shielded glovebox, using a 30 kV field emission gun (FEG) to enable high-resolution scanning electron imaging. The employed analytical system was equipped with two main imaging detectors; an Everhart-Thornley Detector (ETD) for the collection of secondary electrons (SE) and a Circular Backscatter Sensor (CBS) for electron-backscatter images and a spectrometric system for Electron Dispersive Spectroscopy (EDS) based on a Bruker EDS XFlash 6/30 silicon drift detector.

Materials Characterization—Chemical Analyses: The final carbon content was determined in a modified gas analyzer CS-800 from ELTRA GmbH, using the infrared absorption detection technique.

Materials Characterization—Evaluation of the Specific Surface Area: The SSA was evaluated via the Brunauer-Emmet-Teller (BET) method from N_2 physisorption isotherms at 77.3 K collected with a surface area analyzer (Gemini VII Version 5.03, Micromeritics) in the range 0.05 – 0.30 p/p_0.

Supporting Information

Supporting Information is available from the Wiley Online Library or from the author.

Acknowledgements

Conflict of Interest

The authors declare no conflict of interest.

Data Availability Statement

The data that support the findings of this study are available from the corresponding author upon reasonable request.

Keywords

[1] D. Gu, X. Shi, R. Poprawe, D. L. Bourell, R. Setchi, J. Zhu, *Science* **2021**, *372*, abg1487.

[2] H. Li, T. Yue, F. Zhu, Y. Peng, Y. Li, C. Huang, Y. Zhang, in: *Proc. of the 2021 28th Int. Conf. on Nuclear Engineering, ICONE*, Vol. 2. **2021**, https://doi.org/10.1115/ICONE28-65776.

[3] G. Christopher, *Strateg. Trade Rev.* **2015**, *1*.

[4] C. Hensley, K. Sisco, S. Beauchamp, A. Godfrey, H. Rezayat, T. McFalls, D. Galicki, F. List, K. Carver, C. Stover, D. W. Gandy, S. S. Babu, *J. Nucl. Mater.* **2021**, *548*, 152846.

[5] B. R. Betzler, B. J. Ade, A. J. Wysocki, M. S. Greenwood, J. J. W. Heineman, P. C. Chesser, P. K. Jain, F. Heidet, A. Bergeron, *Int. Conf. Phys. React. Transit. to a Scalable Nucl. Futur. PHYSOR* **2020**, *2020*, 01011.

[6] A. T. Nelson, *Prog. Nucl. Energy* **2023**, *155*, 104493.

[7] J. M. Harp, H. J. M. Chichester, L. Capriotti, *J. Nucl. Mater.* **2018**, *509*, 377.

[8] A. Breda, A. Zanini, A. Campagnolo, S. Corradetti, M. Manzolaro, G. Meneghetti, P. Colombo, M. Ballan, G. Franchin, *Ceram. Int.* **2023**, *49*, 31666.

[9] H. N. G. Wadley, D. T. Queheillalt, *Mater. Sci. Forum* **2007**, https://doi.org/10.4028/0-87849-428-6.242.

[10] A. Burke, *Uranium*, 1st ed., John Wiley & Sons, Hoboken, NJ **2017**.

[11] B. M. T. C. Peluzo, E. Kraka, *Int. J. Mol. Sci.* **2022**, *23*, 4655.

[12] D. Yun, M. Stan, *J. Mater. Res.* **2013**, *28*, 2308.

[13] W. T. Thompson, B. J. Lewis, E. C. Corcoran, M. H. Kaye, S. J. White, F. Akbari, Z. He, R. Verrall, J. D. Higgs, D. M. Thompson, T. M. Besmann, S. C. Vogel, *Zeitschrift Fuer Met. Res. Adv. Tech.* **2007**, *1004*, 101556.

[14] C. Degueldre, D. T. Goddard, G. Berhane, A. Simpson, C. Boxall, *J. Nucl. Mater.* **2022**, *562*, 153612.

[15] A. R. Wagner, J. M. Harp, K. E. Archibald, S. C. Ashby, J. K. Watkins, K. R. Tolman, *MethodsX* **2019**, *6*, P1252.

[16] G. Vasudevamurthy, T. W. Knight, *Nucl. Technol.* **2008**, *163*, 321.

[17] G. Vasudevamurthy, A. T. Nelson, *J. Nucl. Mater.* **2022**, *558*, 153145.

[18] L. Grande, B. Villamere, L. Allison, S. Mikhael, A. Rodriguez-Prado, I. Pioro, *J. Eng. Gas Turbines Power* **2011**, *133*, 022901.

[19] S. Dhoundiyal, S. Srivastava, S. Kumar, G. Singh, S. Ashique, R. Pal, N. Mishra, F. Taghizadeh-Hesary, *Eur. J. Med. Res.* **2024**, *29*, 26.

[20] M. Grzmil, A. Meisel, M. Behé, R. Schibli, *Radiopharm. Chem.* **2019**, 85.

[21] A. Gottberg, *Nucl. Instruments Methods Phys. Res. Sect. B Beam Interact. with Mater. Atoms* **2016**, *376*, 8.

[22] L. Biasetto, S. Corradetti, S. Carturan, R. Eloirdi, P. Amador-Celdran, D. Staicu, O. D. Blanco, A. Andrighetto, *Sci. Rep.* **2018**, *8*, 8272.

[23] A. Andrighetto, M. Tosato, M. Ballan, S. Corradetti, F. Borgna, V. Di Marco, G. Marzaro, N. Realdon, *J. Radioanal. Nucl. Chem.* **2019**, *322*, 73.

[24] S. Corradetti, L. Biasetto, M. Manzolaro, D. Scarpa, S. Carturan, A. Andrighetto, G. Prete, J. Vasquez, P. Zanonato, P. Colombo, C. U. Jost, D. W. Stracener, *Eur. Phys. J. A* **2013**, *49*, 56.

[25] V. N. Panteleev, O. Alyakrinskiy, M. Barbui, A. E. Barzakh, M. Dubois, C. Eleon, S. Essabaa, D. V. Fedorov, G. Gaubert, A. M. Ionan, V. S. Ivanov, P. Jardin, C. Lau, R. Leroy, G. Lhersonneau, K. A. Mezilev, C. Mhamed, P. L. Molkanov, F. V. Moroz, S. Y. Orlov, M. G. Saint Laurent, L. Stroe, L. B. Tecchio, M. Tonezzer, A. C. C. Villari, Y. M. Volkov, *Nucl. Instruments Methods Phys. Res. Sect. B Beam Interact. with Mater. Atoms* **2008**, *266*, 4247.

[26] S. Tusseau-Nenez, B. Roussière, N. Barré-Boscher, A. Gottberg, S. Corradetti, A. Andrighetto, M. Cheikh Mhamed, S. Essabaa, H. Franberg-Delahaye, J. Grinyer, L. Joanny, C. Lau, J. Le Lannic, M. Raynaud, A. Saïd, T. Stora, O. Tougait, *Nucl. Instruments Methods Phys. Res. Sect. B Beam Interact. with Mater. Atoms* **2016**, *370*, 19.

[27] G. D. Alton, J. C. Bilheux, A. D. McMillan, *Nucl. Instruments Methods Phys. Res. Sect. A Accel. Spectrometers, Detect. Assoc. Equip.* **2004**, *521*, 108.

[28] M. Cervantes, P. Fouquet-Métivier, P. Kunz, L. Lambert, A. Mjos, T. Day Goodacre, J. Wong, A. Gottberg, *Nucl. Instruments Methods Phys. Res. Sect. B Beam Interact. with Mater. Atoms* **2020**, *463*, 367.

[29] D. W. Stracener, G. D. Alton, R. L. Auble, J. R. Beene, P. E. Mueller, J. C. Bilheux, *Instruments Methods Phys. Res. Sect. A Accel. Spectrometers, Detect. Assoc. Equip.* **2004**, *521*, 126.

[30] J. Guillot, B. Roussière, S. Tusseau-Nenez, D. S. Grebenkov, M. Ignacio, *Nucl. Instruments Methods Phys. Res. Sect. B Beam Interact. with Mater. Atoms* **2020**, *468*, 1.

[31] J. P. Ramos, *Nucl. Instruments Methods Phys. Res. Sect. B Beam Interact. with Mater. Atoms* **2020**, *463*, 201.

[32] X. Zhang, P. Li, M. Krzyaniak, J. Knapp, M. R. Wasielewski, O. K. Farha, *Inorg. Chem.* **2020**, *59*, 16795.

[33] C. K. Jørgensen, R. Reisfeld, *Structure and Bonding* **2005**, *50*, 121.

[34] H. D. Burrows, T. J. Kemp, *Chem. Soc. Rev.* **1974**, *3*, 139.

[35] A. Blanes Díaz, D. V. Kravchuk, A. A. Peroutka, E. Cole, M. C. Basile, T. Z. Forbes, *Eur. J. Inorg. Chem.* **2021**, *2021*, 166.

[36] J. G. West, T. A. Bedell, E. J. Sorensen, *Angew. Chemie – Int. Ed.* **2016**, *55*, 8923.

[37] S. Choi, S. Lee, J. Jeon, J. An, S. B. Khan, S. Lee, J. Seo, H. Han, *J. Appl. Polym. Sci.* **2010**, *117*, 2937.

[38] A. Nakayama, Y. Kumamoto, M. Minoshima, K. Kikuchi, A. Taguchi, K. Fujita, *Adv. Opt. Mater.* **2022**, *10*, 2200474.

[39] A. Jagtap, A. More, *Polym. Bull.* **2022**, *79*, 8057.

[40] T. Rosental, S. Mizrahi, A. Kamyshny, S. Magdassi, *Virtual Phys. Prototyp.* **2021**, *16*, 255.

[41] E. Shukrun, I. Cooperstein, S. Magdassi, *Adv. Sci.* **2018**, *5*, 1800061.

[42] I. Cooperstein, E. Shukrun, O. Press, A. Kamyshny, S. Magdassi, *ACS Appl. Mater. Interfaces* **2018**, *10*, 18879.

[43] M. Y. Moshkovitz, D. Paz, S. Magdassi, *Adv. Mater. Technol.* **2023**, *8*, 2300123.

[44] E. Shukrun Farrell, Y. Schilt, M. Y. Moshkovitz, Y. Levi-Kalisman, U. Raviv, S. Magdassi, *Nano Lett.* **2020**, *20*, 6598.

[45] G. Franchin, H. Elsayed, R. Botti, K. Huang, J. Schmidt, G. Giometti, A. Zanini, A. De Marzi, M. D'Agostini, P. Scanferla, Y. Feng, P. Colombo, *Chinese J. Mech. Eng. Addit. Manuf. Front.* **2022**, *1*, 100012.

[46] A. Vyatskikh, S. Delalande, A. Kudo, X. Zhang, C. M. Portela, J. R. Greer, *Nat. Commun.* **2018**, *9*, 593.

[47] D. W. Yee, M. A. Citrin, Z. W. Taylor, M. A. Saccone, V. L. Tovmasyan, J. R. Greer, *Adv. Mater. Technol.* **2021**, *6*, 2000791.

[48] D. W. Yee, M. L. Lifson, B. W. Edwards, J. R. Greer, *Adv. Mater.* **2019**, *31*, 1901345.

[49] M. A. Saccone, R. A. Gallivan, K. Narita, D. W. Yee, J. R. Greer, *Nature* **2022**, *612*, 685.

[50] M. Pechini, (United States Pat. Off.), *Patent No.3 330 697*, **1967**.

[51] D. Salvato, J. F. Vigier, O. Dieste Blanco, L. Martel, L. Luzzi, J. Somers, V. Tyrpekl, *Ceram. Int.* **2016**, *42*, 16710.

[52] B. S. Barros, R. Barbosa, N. R. Dos Santos, T. S. Barros, M. A. Souza, *Inorg. Mater.* **2006**, *42*, 1348.

[53] M. P. Pechini, *Method of preparing lead and alkaline earth titanates and niobates and coating method using the same to form a capacitor,* US Patent No. 3330697, **1967**.

[54] R. N. Goldberg, Y. B. Tewari, J. C. Ahluwalia, *J. Biol. Chem.* **1989**, *264*, 9901.

[55] E. A. Souza, J. G. S. Duque, L. Kubota, C. T. Meneses, *J. Phys. Chem. Solids* **2007**, *68*, 594.

[56] A. Alhaji, R. S. Razavi, A. Ghasemi, M. R. Loghman-Estarki, *Ceram. Int.* **2017**, *43*, 2541.

[57] A. Zanini, S. Corradetti, S. M. Carturan, P. Colombo, A. Andrighetto, G. Franchin, *Microporous Mesoporous Mater.* **2022**, *317*, 11917.

[58] M. Azam, S. I. Al-Resayes, A. Trzesowska-Kruszynska, R. Kruszynski, P. Kumar, S. L. Jain, *Polyhedron* **2017**, *124*, 177.

[59] J. Kretzschmar, S. Tsushima, C. Lucks, E. Jäckel, R. Meyer, R. Steudtner, K. Müller, A. Rossberg, K. Schmeide, V. Brendler, *Inorg. Chem.* **2021**, *60*, 7998.

[60] W. Hummel, G. Anderegg, L. Rao, I. Puigdomènech, O. Tochiyama, *Chemical Thermodynamics of Compounds and Complexes of U, Np, Pu, Am, Tc, Se, Ni and Zr with Selected Organic Ligands*, NEA-OECD, Elsevier, Amsterdam **2005**.

[61] G. Meinrath, Y. Kato, T. Kimura, Z. Yoshida, *Radiochim. Acta* **1998**, *82*, 115.

[62] G. Meinrath, D. Kwiatek, Z. Hnatejko, S. Lis, *Monatshefte Fur Chemie* **2014**, *145*, 1689.

[63] M. Karbowiak, B. Fourest, S. Hubert, C. Moulin, *Radiochim. Acta* **2003**, *91*, https://doi.org/10.1524/ract.91.9.505.20002.

[64] A. Chaumont, O. Klimchuk, C. Gaillard, I. Billard, A. Ouadi, C. Hennig, G. Wipff, *J. Phys. Chem. B* **2012**, *116*, 3205.

[65] S. Berto, F. Crea, P. G. Daniele, C. De Stefano, E. Prenesti, S. Sammartano, *Radiochim. Acta* **2012**, *100*, 22.

[66] M. Glorius, H. Moll, G. Bernhard, *Radiochim. Acta* **2007**, *95*, 156.

[67] G. Meinrath, *Radiochim. Acta* **1997**, *77*, 226.

[68] F. Quilès, C. Nguyen-Trung, C. Carteret, B. Humbert, *Inorg. Chem.* **2011**, *50*, 2811.

[69] S. P. Pasilis, J. E. Pemberton, *Inorg. Chem.* **2003**, *67*, 6793 .

[70] M. R. Duff, C. V. Kumar, *Angew. Chemie – Int. Ed.* **2005**, *45*, 137.

[71] R. L. B. Elnegaard, N. E. Møllegaard, Q. Zhang, F. Kjeldsen, T. J. D. Jørgensen, *ChemBioChem* **2017**, *18*, 1117.

[72] J. Guillot, S. Tusseau-Nenez, B. Roussière, N. Barré-Boscher, F. Brisset, S. Denis, *Nucl. Instruments Methods Phys. Res. Sect. B Beam Interact. with Mater. Atoms* **2018**, *33*, 60.

[73] S. Chowdhury, L. Maria, A. Cruz, D. Manara, O. Dieste-Blanco, T. Stora, A. P. Gonçalves, *Nanomaterials* **2020**, *10*, 2458.

[74] S. K. Mukerjee, J. V. Dehadraya, V. N. Vaidya, D. D. Sood, *J. Nucl. Mater.* **1994**, *210*, 2458.

[75] D. P. STINTON, S. M. TIEGS, W. J. LACKEY, T. B. LINDEMER, *J. Am. Ceram. Soc.* **1979**, *62*, 596.

[76] M. A. Pimenta, G. Dresselhaus, M. S. Dresselhaus, L. G. Cançado, A. Jorio, R. Saito, *Phys. Chem. Chem. Phys.* **2007**, *9*, 1276.

[77] J. Guillot, B. Roussière, S. Tusseau-Nenez, N. Barré-Boscher, E. Borg, J. Martin, *Nucl. Instruments Methods Phys. Res. Sect. B Beam Interact. with Mater. Atoms* **2017**, *394*, 153.

[78] A. L. Patterson, *Phys. Rev.* **1939**, *56*, 978.